Article:

Buente, D, Bryant, M orcid.org/0000-0003-4442-5169, Ward, M et al. (3 more authors) (2017) The taper corrosion pattern observed for one bi-modular stem design is related to geometry-determined taper mechanics. Medical Engineering & Physics, 46. pp. 79-88. ISSN 1350-4533

https://doi.org/10.1016/j.medengphy.2017.06.003

The Taper Corrosion Pattern Observed for One Bi-Modular Stem Design is Related to Geometry-Determined Taper Mechanics

AUTHORS, CONTACT DETAILS, AND AFFILIATIONS

Dipl.-Ing Dennis Bünte[1*], dennis.buente@tuhh.de

Dr. Michael Bryant[2], m.g.bryant@leeds.ac.uk

Dr. Michael Ward[2], m.b.ward@leeds.ac.uk

Prof. Anne Neville[2], a.neville@leeds.ac.uk

Prof. Michael Morlock[1] morlock@tuhh.de

Dr. Gerd Huber[1], g.huber@tuhh.de

*corresponding author

[1]TUHH Hamburg University of Technology
Institute of Biomechanics, Denickestrasse 15
21073 Hamburg, Germany

[2]University of Leeds,
Faculty of Engineering
Institute of Materials and Research/ Functional Surfaces,
Leeds LS2 9JT, UK

KEYWORDS

Taper Mechanics, Geometrical Mismatch, Design, Failure Mechanism, Wear Pattern, Fretting Corrosion

ABSTRACT

Bi-modular primary hip stems exhibit high revision rates owing to corrosion at the stem-neck taper, and are associated with local adverse tissue reactions. The aim of this study was to relate the wear patterns observed for one bi-modular design to its design-specific stem-neck taper geometry.

Wear patterns and initial geometry of the taper junctions were determined for 27 retrieved bi-modular primary hip arthroplasty stems (Rejuvenate, Stryker Orthopaedics) using a tactile coordinate-measuring device. Regions of high-gradient wear patterns were additionally analyzed via optical and electron microscopy.

The determined geometry of the taper junction revealed design-related engagement at its opening (angle mismatch), concentrated at the medial and lateral apexes (axes mismatch). A patch of retained topography on the proximal medial neck-piece taper apex was observed, surrounded by regions of high wear. On the patch, a deposit from the opposing female stem taper —containing Ti, Mo, Zr, and O—was observed .

High stress concentrations were focused at the taper apexes owing to the specific geometry. A medial canting of the components may have augmented the inhomogeneous stress distributions *in vivo*. In the regions with high normal loads interfacial slip and consequently fretting was inhibited, which explains the observed pattern of wear.

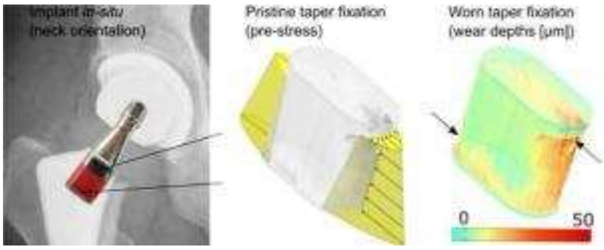

INTRODUCTION

Total hip replacements with modular necks show an increased risk for early failure [1]. Clinical failures range from neck fracture [2–6] to symptomatic adverse tissue reactions [7–9]. Early failures of one specific design (Rejuvenate, Stryker Orthopaedics, Mahwah, New Jersey) were linked to fretting-corrosion and substantial wear from the bi-modular neck-piece taper ~~(CoCrMo)~~ [10–16]. The system was consequently recalled [17]. A recent study demonstrated that sections with high local *in vivo* loads exhibited distinct material loss from the CoCrMo neck pieces [18]. An implant specific failure mechanism was suggested because a distinct and evolving wear pattern was observed on the cohort of retrieved neck pieces ($CoCr_{29}Mo_6$, hereafter referred to as CoCrMo; Figure 1), whereas the Titanium-alloy counterparts ($TiMo_{12}Zr_6Fe_2$, hereafter referred to as TMZF) remained without a notable wear pattern [19].

Mechanically assisted corrosion had been identified as the dominant mechanism for material loss from conical metallic tapers *in vivo* [19,20], which may be a concern for implant survivorship of modern hip implant designs [21–23]. The mechanical damage of native oxide layers initiates the corrosive attack of otherwise inert components [24–26]. Thus, local relative motions and insufficient normal stress at the contact interface are considered mechanical prerequisites for taper wear [27].

The determining risk factors of the degradation processes *in vivo* are multifactorial [14,28,29] and still largely debated. However, the initial mechanical condition at the junction is thought to determine the initiation and progression of the degradation of taper interfaces [30,31].

The mechanical contact situation within tapers can be seen as a superimposition of 1) the permanent normal pre-stress from the elastic strain that occurred from the assembly of the taper, and 2) the temporally applied stresses caused by applied joint loads. The taper geometry and its implant-specific orientation with respect to the joint load predetermine the contact stress configuration. Relative motion will occur, if the interfacial shear stress exceeds the available frictional shear stress provided by the local normal pre-stress. This imbalance can be attributed to a variety of factors, such as the design (taper geometry, clearances between male and female tapers, taper orientation, and taper materials [32,33]), the assembly conditions (assembly force and taper contamination [34]), or surgical and patient-specific factors (surgical techniques and activity levels [35]).

Within circular tapers, the contact configuration between the male and female taper can be mainly described by their angular mismatch (ASTM F3129-16). The angular mismatch predicts the location of the ideally ring-shaped engagement, and is consequently considered as an important parameter for the taper function [36–39]. Non-circular taper geometries, which are common in bi-modular implants, incorporate additional shape parameters (Figure 2) and additional strategies for adjusting the mismatches [40]. The geometry and clearances of the tapers could be attuned to provide the required pre-stress to transmit the expected loading *in vivo*

[23]. However, this adaption might miss the real clinical situation, which could be the reason why certain bi-modular tapers appeared to be less robust [12,13,23,41–43].

This study aims to explain the wear pattern of one specific taper design with trigonometric considerations of male and female taper geometries.

MATERIALS AND METHODS

Cohorts of new and retrieved bi-modular hip replacements (2 new stems, 4 new neck pieces, 27 explanted stems and corresponding neck pieces of the Rejuvenate modular hip system) were available for analysis. The retrieved implants were revised owing to adverse tissue reactions between 2.9 and 38.1 months after their implantation (see Table 1; further patient and cohort details can be found in our previous research work [18]). After obtaining informed consent of the patient, the retrieved implants were manually cleaned with an ethanol-immersed cloth, and were then exposed to an ultrasound bath (Elmasonic P, Elma Schmidbauer GmbH, Singen, Germany) with soap (Edisonite 5%, Schülke & Mayr GmbH, Norderstedt, Germany). Male neck-piece tapers and female stem tapers of the retrieved and the new tapers were measured via a point-by-point method using a tactile coordinate-measuring device (Mitutoyo BHN 805, Tokyo, Japan; 3 µm precision; scanning grid: 0.5 mm x 0.5 mm or 0.1 mm x 0.1 mm). The measurements were obtained using a Ruby sphere with a diameter of 2 mm.

The female tapers were mostly damaged by longitudinal rupture marks at their lateral apexes, which had been likely caused by revision tools. The male tapers were worn (material loss of 3.35 ± 1.83 mm^3, ranging from 0.55 to 7.57 mm^3); however, distally and proximally they exhibited pristine, non-contact bands. These unworn areas were exploited for the reconstruction of the initial, pristine tapers. For two retrievals, the aforementioned areas were mechanically damaged during explantation; therefore, the components were completely excluded from further analysis.

Estimated original taper geometry: In order to understand the contact mechanics of the taper interface and its relation to the observed wear patterns, the original taper geometry must be determined. The male and female taper geometries of the analyzed bi-modular taper design may be described as two separated parallel conical sections (180° each) that are connected by planes (Figure 3). The distance between the two cone axes, and a global taper angle averaged within the conical sections were used for the parametrization of each taper.

Both conical sections were approximated by horizontal roundness and vertical straightness profiles (ASTM F3129-16) fitted onto the 3D data cloud from the tactile measurements. In the transverse direction, the roundness profiles were made available by fitting circles to the left and right conical sections at every height level (least squares fits; height resolution of 0.02 mm). By equalizing the radii between the two conical sections, the location of the adjusted reference systems of left and right conical section were iteratively computed. This computation yielded the distance of the two conical axes (d). The global orientation was determined via slopes that were fitted around the taper circumference of the two conical sections (500 equally spaced slopes per side). By iteratively reducing the opposing angles, the reference system was aligned. The pristine taper geometries were recovered from the results of tactile measurements by the interpolation between the two non-contact bands (male tapers only). The root mean-square errors indicated local deviations from one-dimensional profile (e.g., by wear). Dependent on the wear extent, 50 to 70% of the best slopes and semi-circles were used for the reconstruction of the taper axes. The inclination of the local slopes from the conical sections yielded local taper angles, hereafter denoted as α_i. The local variations from the connecting planes were not further quantified. The spread of the local taper angles ($\Delta\alpha$) around the circumference of the male and female tapers was recorded.

Apart from the distance between the axes of the conical sections, a global taper angle $\bar{\alpha}$ was computed by averaging the available local taper angles of both conical sections.

A pilot study of three randomly selected explants revealed the repeatability of the method, for sampling distances of 0.1 and 0.5 mm. Within 10 iterations, the alignment residuals fell below an accuracy threshold (0°0′18″ for orientations; 0.01 µm for offsets). Female taper geometries were reproduced for the coarser 0.5 mm × 0.5 mm grid (test–retest error of $\bar{\alpha}$ = 1′6″ ± 0′18″, d = 2.5 ± 1 µm). The male tapers exhibited higher wear; consequently, they required sufficient measurement points within the non-contact bands. Thus, a narrow measurement sampling distance of 0,1 mm was used (reproducible test–retest error $\bar{\alpha}$ = 0′6 ″ ± 0′12″, d = 0.7 ± 1 µm).

The angular mismatch (A) and the mismatch of the distances of the conical axes (D) between male and female tapers were determined by calculating the difference of their respective values (Equations 1 and 2).

$$A = \bar{\alpha}_{male} - \bar{\alpha}_{female} \quad (1)$$

$$D = d_{male} - d_{female} \quad (2)$$

To create the control group, new implants were randomly combined for all permutations (n = 8) to obtain corresponding values.

Taper engagement model: Based on the estimation of the original taper geometry, a trigonometric-taper engagement model was created. It was assumed that the materials of the tapers elastically deformed within the contact interface, and that the computed clearances dominated the contact stress at the taper interface. The theoretical contact mechanics of the analyzed taper design can thus be categorized according to the taper clearance parameters (Figure 4): The angular mismatch (A) describes the pre-stress distribution in the longitudinal direction (throat contact vs. mouth contact, as defined in the ASTM F3129-16). The axes mismatch (D) describes its characteristics in the transverse direction (apex contact vs. flat contact). The initial gap dimensions were estimated for different seating depths (S) through trigonometric relationships of the determined taper geometries. Negligible deformation of the components at the non-contact regions was assumed. However, it has to be mentioned that incongruent taper surfaces subjected to high bending loads may cause the male and female taper components to be vulnerable to canting. This would result in a pre-stress distribution different from the one predicted via the taper geometries alone (Figure 4). A large degree of tilting might even overcome angular clearances and may lead to a diagonally pre-stress orientation with an even higher stress concentration.

Taper wear analysis: Assuming that wear is related to the mechanical contact situation, the taper clearances will be replicated in the typical wear pattern. In addition to tactile taper wear analyses that were previously conducted for the cohort [18], the wear patterns of the neck-piece tapers in proximity of the original surface patches were analyzed via microscopic techniques (Figure 1).

Infinite focus microscopy (Alicona InfiniteFocus, Alicona, Austria) was employed for the quantification of the topographies around the high-wear regions near the medial apexes, proximally to the retrieved tapers (Figure 1; ×10 magnification, lateral resolution of 2 µm, and vertical resolution of 0.5 µm). The surface heights of the local patches within the high-wear regions were quantified by leveling them to heights of adjacent, proximal non-contact areas. The patch dimensions, texture quality, and deposits were recorded and its positions were determined by mapping the optical images to wear patterns from the global tactile method (Figure 1).

One neck piece with a highly developed wear pattern (Figure 1; Patient 4 (Table 1), material loss of 5.29 mm^3; [18]) was available for destructive testing. It was selected for advanced electron microscopy (scanning electron microscopy (SEM), Zeiss Supra 55 VP, Carl Zeiss AG, Germany; transmission electron microscopy (TEM), FEI Tecnai F20 FEG-TEM/Oxford Instruments X-Max SDD–EDX detector).

A focused ion beam (FIB) system (FEI Nova 200 NanoLab dual beam SEM/FIB; the method has been described in past research works [44]) was used for the determination of the material characteristics from differently worn locations within the taper contact regions (sites I–III, Figure 5). For the purposes of comparison, a proximal non-contact location was additionally analyzed (site IV). At one site, the element composition throughout an interfacial layer was recorded (site II).

The geometrical taper parameters were statistically analyzed; the analysis was conducted using the one-way analysis of variances technique and the Mann–Whitney U-test (IBM Corp., SPSS Statistics, Armonk, New York, USA). The probability of a Type I error was set to 5%.

RESULTS

Estimated original taper geometry and location of taper engagement: The global taper angles were similar among retrievals and new implants (differences < 1′; Table 2). The retrieved female tapers presented the highest variation in global taper angles. The spread of the local taper angles around the taper circumference was higher for female than for male tapers ($\Delta\alpha_{female}$ = 03′50″ ± 01′00″, $\Delta\alpha_{male}$ = 02′10″ ± 01′10″). Within the cohort of the new implants, the fluctuations of the local taper angle of the male tapers exhibited small spreads ($\Delta\alpha_{male}$ = 01′00″), whereas the new female tapers were the least uniform ($\Delta\alpha_{female}$ = 05′00″).

The angular mismatches (A) were always negative ($A_{retrieved}$ = -03′20″ ± 02′20″, n = 25; A_{new} = -03′00″ ± 00′10″; randomly combined, n = 8), thus resulting in first contact in the throat (Figure 4, right). The mismatch of the distance between the conical axes was always negative ($D_{retrieved}$ = -21.5 ± 10.3 µm; D_{new} = 16.1 ± 5.0 µm), thus resulting in taper engagement at their apexes (Figure 4, left). Between the new and the retrieved components, no significant differences were found in the taper angle mismatch ($p = 0.27$) or the axes mismatch ($p = 0.07$). Assuming elastic deformation only, the trigonometric model showed that increasing seating depth will result in a growth of the contact areas from the throat to the mouth of the tapers, beginning at the apexes of the conical sections (first contact). The proximal gaps at the flat sides close only when the apexes are fully in contact (Table 3).

Taper wear: The infinite focus microscopy from the medial apexes of the male tapers revealed a high-gradient wear pattern at the proximal taper opening (Figure 1). Surrounded by worn areas, characteristic patches with preserved original texture were discovered (Figure 5). These patches appeared to have remained unchanged from the wear process. Their maximal surface heights deviated less than ±5 µm from those of the proximal non-contact regions. Although a few patches were only partially exposed to the worn surrounding (n = 5; material loss < 2.3 mm^3) or multiple patches appeared (n = 3), most explants (n = 18) presented singular patches that were completely surrounded by deep wear and shiny texture (site III, wear depth > 40 µm). These patches all covered the medial apexes of the tapers, and their centers had slightly shifted toward the taper anterior (patch width: 700 ± 400 µm; the patches on the left implants shifted clockwise, whereas the right implants shifted anti-clockwise by 140 ± 90 µm). Pristine surface texture with horizontal manufacturing lines was identified on proximal regions on the patches (Figure 5, insert; Figure 6). Furthermore, singular deposits were observed in this region. More distally, patches were densely covered by bulk deposit. In these regions, vertical scratches and other marks that were probably caused during disassembly were observed .

Subsurface measurements from a location of high-wear depths (site III) and from two locations on the proximal patch (preserved surface or deposit; corresponding sites I or II, respectively) were compared to a non-contact location on the same taper (site IV; Figure 5). For the non-contact location, crystalline layers were observed that transitioned to larger grains as the depths become greater (Figure 7). Deep wear had left behind large undistorted grains at the surface. On the patch, crystalline layers were found of comparable thickness to the non-contact location. Collective grain orientation was observed at the 500 µm subsurface zone (Figure 8). The element analysis across the interface between the CoCrMo patch and the deposit revealed attached responsive elements in the ratios of the TMZF alloy [45] onto the CoCrMo bulk neck-piece material [46]. The line scan (100 µm wide) shows how Co and Cr abruptly decline when TMZF elements (Titanium, Molybdenum, Zirconium, iron) become responsive. Cobalt does not fully fade out within the deposit. At the interface, Oxygen was only responsive in 100 nm widths (Figure 9).

DISCUSSION

This paper presents a mechanical model to describe the implant-specific failure modes of bi-modular hip prostheses. The determined *in vivo* contact mechanics, based on the taper angles and axes, could explain the distinct pattern of extensive wear and corrosion that were observed consistently on retrieved implants.

Taper design: For the analyzed design, geometrical mismatches predict taper engagement at the taper throat (distal) at the apexes of the conical sections (medial-lateral). Gaps on the flat sides persist on the µm-scale, if the taper is not seated to full contact (Table 3). The designed axes mismatch (D) predicts considerable engagement of the conical apexes. If the local straining of the taper directly translates into contact stress, the taper assembly will generate permanent concentrations of normal contact stress at the apexes of the conical taper sections (Figure 10a). The normal contact stress diminishes quickly to the anterior and posterior flat sides.

The distances of the axes among analyzed male and female tapers (d) varied in the order of magnitude of axes mismatches of their corresponding taper junctions (D; µm scale). Local taper angles (α_i) spread in the order of magnitude of angular mismatches (A) of their corresponding taper junctions. Thus, variations in taper geometry between pristine implants could largely influence the distribution of contact stress, hence adding up to the individual risk for local taper corrosion.

In vivo loads applied within the longitudinal plane containing both taper apexes are transmitted effectively, as the loading coincides with the designed high pre-stress at the apexes of the conical sections (Figure 10b). Loads with an offset to this symmetry plane create oblique bending, which is not as efficiently transmitted (Figure 10c). If the taper had not been seated to full contact, it is possible that the elastic deformation of the implant components under cyclic loading would have caused the continuous closing and opening of the gaps and cavities; this could have fostered fluid ingress. In contrast to a circular taper, which does not have a preferred directionality, the taper orientation (e.g., owing to stem anteversion or retroversion) could thus have influenced the extent of micromotions and the development of wear at a distance to the apexes (Figure 5).

Explant analyses: At the time of explantation, the retrieved neck pieces indicated dominant wear from the conical sections, which was arranged diagonally across the taper contact region [18]. Subsurface microscopy offered valuable insight to the dominant degradation mechanisms that were responsible for the local wear depths (Figure 5). The non-contact site revealed a nano-crystalline layer (Figure 7), which is typical for mechanically machined CoCrMo surfaces [46,47]. In proximity to the patch (site III), the microstructure near to the surface coincided with the bulk microstructure, with large grains reaching the surface. This region of high wear appeared as electro-polished, which suggested a corrosion-dominated degradation process; mechanical wear components would have triggered the reformation of an outermost nano-crystalline zone [46,47].

The sample from the patch at the medial taper apex revealed microstructures with high twinning densities and refined grains toward the surface. A nano-crystalline layer directly beneath the surfaces is comparable in thickness with those observed within the non-contact region (Figure 8). Furthermore, the preserved original texture, including the machining marks, can be observed (Figure 5, Figure 6), and the top of the patches are of the same height as the non-contact location. However, at the locations of the preserved original texture on the patch (site I, Figure 6), the grain directionality within the subsurface layers suggests plastic shearing below the crystalline layers (Figure 8). The plasticity was probably induced by high shear stresses [46], which required high normal stresses or adhesive forces at the taper interface. These conditions could prevent fretting corrosion by inhibiting relative motion and access of a medium.

Deposit was apparent on medial patch regions (site I). Subsurface measurements identified TMZF bulk constituents that had attached onto male CoCrMo bulk (Figure 9). This may be explained by high adhesive forces between the CoCrMo and the TMZF, which locally exceeded the disassembly shear and the ultimate strength of the female taper TMZF material. Cobalt is expectedly soluble in this electrochemical context [44]. It was responsive throughout the deposit, thus indicating microscopic damages of the TMZF side, which are not further addressed here. The Oxygen content was only responsive in a 100 nm band at the interface (Figure 9). This suggests a frictional welding phenomenon between the CoCrMo and the TMZF. The role of the oxide and the required permanent loading conditions are yet unclear. It is suspected that this phenomenon is responsible for the local protection against wear, and may depend on the specific material combination [48].

Design performance *in vivo*: The position of no-wear patches on the male taper reflected the location of the engagement of tapers before the *in vivo* wear process had begun. Their position at the taper apexes corresponded to regions of estimated pre-stress concentrations, which had been determined from the negative axes mismatch of the taper design (Figure 10a). The limited patch widths and the high-wear gradients towards the anterior and posterior (Figure 5) reflect the corresponding stress drops at the incongruent apexes. The posterior shifts of the medial no-wear patches reflected the direction of the elastic deformation of the male taper in the direction of the dominant in vivo load, which slightly shifted toward the posterior. Interestingly, no-wear patches medially were consistently observed at the proximal taper mouth, which indicates that the retrievals permanently overcame their angular clearance. Instead of the engaging at the throat (Figure 10a), the tapers had changed the permanent pre-stress to a diagonal engagement (Figure 10b). It was thus suggested that the retrieved taper had seated into a canted position prior to being worn. This indicated that the fixation had been insufficient for a stable transfer of loads with the predicted engagement strategy (Figure 4). The permanent tilting of the taper might impose additional incongruences to the taper contact surfaces that potentially gave rise to local-wear phenomena and the observed wear transitions. Once initiated, these “spacers” prevented a more homogenous contact configuration with smaller crevices (Figure 10d). An increased fretting motion toggling around these fulcrum points was suggested. This may explain the harshening of the environment with excessive galvanic corrosion, which was observed. The engagement features and their robustness against the canting of male and female taper components may thus be considered an important design feature for the prevention of mechanically assisted corrosion.

Reconstructing pristine taper geometries from the data acquired via tactile measurements of worn implants had certain limitations. As female tapers may exhibit contact over their entire surface, it was impossible to completely exclude *in vivo* changes. Nonetheless, the determination of initial taper geometries appeared successful, as the control group of new tapers did not show significantly different taper angles and axes distances; the test–retest errors were comparable for male and female components, despite the observed differences in damage [19]. It could not be determined why new stem tapers presented the highest fluctuations in local taper angles, owing to the limited group of new stems of this design. However, regardless of whether tapers were new or explanted, consistent mismatches (A, $D < 0$) allowed the prediction of a global contact configuration for the analyzed design.

Taper geometries were estimated through first-order approximation only, wherein the surface roughness, the differences in elastic properties, and the textures were not included. The qualitative stress estimates also neglected 3D effects of lateral contraction and contact boundaries. The subsurface analysis was limited to singular sites from one neck piece that was available for destructive testing, which only served as proof of existence of different wear modes. Combined with surface patterns recorded from all neck pieces, the findings were extrapolated to the cohort.

The occurrence of wear phenomena on the taper could be explained by the mechanical conditions predicted at the taper interface; however, the initiation of taper corrosion depended on more factors, which were mostly outside the mechanistic scope of the analysis of the explants. Clinical factors, such as initially low pH in the patient, might have triggered an onset of mechanically assisted corrosion. Such data were unavailable in the explants-based analysis. Moreover, clinical and ethical restrictions impede the availability of control groups with implants that differ by selected design parameters. With regard to design improvements, it is thus difficult to quantify the impact of each of the discussed parameters on the development of tribocorrosion *in vivo*.

Consequently, not every implant of modular prosthesis should be considered as being at a definite risk. Nevertheless, they cannot be considered to be definitely safe, as the onset of the wear mechanism is unclear. However, the awareness of this problem can be clinically useful; it justifies early diagnosis measures for taper wear (magnetic resonance imaging (MRI) and screening of Co and Cr levels) in order to prevent clinical disasters.

CONCLUSIONS

The analyzed taper design engages at the taper apexes, leaving low contact stresses or gaps on the flat sides. The hereby-introduced permanent stress concentrations at the taper apexes are additionally influenced by tolerated manufacturing variances. These factors might contribute to the sensitivity of the design to canting. The engagement strategy appears to be fundamental to local wear phenomena; it facilitated the typical wear transitions in the taper contact zones that formed the characteristic pattern. In regions of permanently high interfacial stress, the material coupling (CoCrMo to TMZF) produced characteristic no-wear patches. The presented taper mechanics may assist in the development of engagement strategies of future taper designs in order to prevent excessive wear and subsequent clinical failure.

CONFLICT OF INTEREST

The corresponding author has no conflicting interests. The co-authors receive research grants from DePuy Synthes, CeramTec, and Peter Brehm. The co-authors are consultants for DePuy and Zimmer Inc. in projects not related to this study.

FUNDING

The research received funding from European Union’s Seventh Framework Program (FP7/2007-2013) grant agreement GA-310477.

ETHICAL APPROVAL

Not required.

ACKNOWLEDGEMENTS

The authors thank Calvin Warriner for providing the explants.

REFERENCES

[1] Orthopaedic Association Australian. National joint replacement registry. Annual Report. 2015.

[2] Krishnan H, Krishnan SP, Blunn G, Skinner JA, Hart AJ. Modular neck femoral stems. Bone Jt J 2013;95 B:1011–21. doi:10.1302/0301-620X.95B8.

[3] Atwood SA, Patten EW, Bozic KJ, Pruitt L, Ries MD. Corrosion-induced fracture of a double-modular hip prosthesis: a case report. J Bone Joint Surg Am 2010;92:1522–5. doi:10.2106/JBJS.I.00980.

[4] Grupp TM, Weik T, Bloemer W, Knaebel H-P. Modular titanium alloy neck adapter failures in hip replacement--failure mode analysis and influence of implant material. BMC Musculoskelet Disord 2010;11:3. doi:10.1186/1471-2474-11-3.

[5] Mencière M-L, Amouyel T, Taviaux J, Bayle M, Laterza C, P M. Fracture of the modular femoral neck component in total hip arthroplasty. Orthop Tramatology Surg Res 2014;100:565–8.

[6] Wright G, Sporer S, Urban R, Jacobs J. Fracture of a Modular Femoral Neck After Total Hip Arthroplasty: A Case Report. JBJS Case Connect 2010;os-92:1518–21. doi:10.2106/JBJS.I.01033.

[7] Burge AJ, Gold SL, Lurie B, Fields KG, Koff MF, Westrich G, et al. MR Imaging of Adverse Local Tissue Reactions around Rejuvenate Modular Dual-Taper Stems. Radiology 2015;277:142–50.

[8] Dimitriou D, Han M, Liow L, Tsai T, Leone WA, Li G, et al. Early Outcomes of Revision Surgery for Taper Corrosion of Dual Taper Total Hip Arthroplasty in 187 Patients. J Arthroplasty 2016;31:1549–54. doi:10.1016/j.arth.2016.01.015.

[9] Cooper HJ, Urban RM, Wixson RL, Meneghini RM, Jacobs JJ. Adverse local tissue reaction arising from corrosion at the femoral neck-body junction in a dual-taper stem with a cobalt-chromium modular neck. J Bone Joint Surg Am 2013;95:865–72. doi:10.2106/JBJS.L.01042.

[10] Meftah M, Haleem AM, Burn MB, Smith KM, Incavo SJ. Early corrosion-related failure of the rejuvenate modular total hip replacement. J Bone Joint Surg Am 2014;96:481–7. doi:10.2106/JBJS.M.00979.

[11] Gkagkalis G, Mettraux P, Omoumi P, Mischler S, Rüdiger HA. Adverse tissue reaction to corrosion at the neck-stem junction after modular primary total hip arthroplasty. Orthop Traumatol Surg Res 2015:4–7. doi:10.1016/j.otsr.2014.11.003.

[12] Lanting B, Teeter M, Vasarhelyi E, Ivanov T, Howard J, Naudie D. Correlation of Corrosion and Biomechanics in the Retrieval of a Single Modular Neck Total Hip Arthroplasty Design: Modular Neck Total Hip Arthroplasty System. J Arthroplasty 2014:1–6. doi:10.1016/j.arth.2014.06.009.

[13] Werner SD, Bono J V, Nandi S, Ward DM, Talmo CT. Adverse tissue reactions in modular exchangeable neck implants: a report of two cases. J Arthroplasty 2013;28:543.e13–5. doi:10.1016/j.arth.2012.07.026.

[14] De Martino I, Assini JB, Elpers ME, Wright TM, Westrich GH. Corrosion and Fretting of a Modular Hip System: A Retrieval Analysis of 60 Rejuvenate Stems. J Arthroplasty 2015:1–6. doi:10.1016/j.arth.2015.03.010.

[15] Pivec R, Meneghini RM, Hozack WJ, Westrich GH, Mont MA. Modular taper junction corrosion and failure: how to approach a recalled total hip arthroplasty implant. J Arthroplasty 2014;29:1–6. doi:10.1016/j.arth.2013.08.026.

[16] Ghanem E, Ward DM, Robbins CE, Nandi S, Bono J V, Talmo CT. Corrosion and Adverse Local Tissue Reaction in One Type of Modular Neck Stem. J Arthroplasty 2015;30:1787–93. doi:10.1016/j.arth.2015.04.039.

[17] No authors listed. Recall notice Rejuvenate. Jt Prosthesis, Hip Femoral Stem ABGII Modul Stems ABGII Modul Necks Rejuvenate Modul Stems Rejuvenate Modul Necks 2012. http://www.mhra.gov.uk/home/groups/fsn/ (accessed May 10, 2013).

[18] Buente D, Huber G, Bishop N, Morlock M. Quantification of material loss from the neck piece taper junctions of a bimodular primary hip prosthesis. A retrieval study from 27 failed Rejuvenate bimodular hip arthroplasties. Bone Jt J 2015;97B:1350–7. doi:10.1302/0301-620X.97B10.35342.

[19] Bryant MG, Buente D, Oladokun A, Ward M, Huber G, Morlock M, et al. Surface and subsurface changes as a result of tribocorrosion at the stem-neck interface of bi-modular prosthesis. Biotribology 2017. doi:10.1016/j.biotri.2017.02.002.

[20] Gilbert JL, Buckley CA, Jacobs JJ. In vivo corrosion of modular hip prosthesis components in mixed and similar metal combinations. The effect of crevice, stress, motion, and alloy coupling. J Biomed Mater Res 1993;27:1533–44. doi:10.1002/jbm.820271210.

[21] Cooper HJ, Della Valle CJ, Jacobs JJ. Biologic implications of taper corrosion in total hip arthroplasty. Semin Arthroplasty 2012;23:273–8. doi:10.1053/j.sart.2013.01.013.

[22] Cook RB, Bolland BJRF, Wharton J a, Tilley S, Latham JM, Wood RJK. Pseudotumour formation due to tribocorrosion at the taper interface of large diameter metal on polymer modular total hip replacements. J Arthroplasty 2013;28:1430–6. doi:10.1016/j.arth.2013.02.009.

[23] Gill IPS, Webb J, Sloan K, Beaver RJ. Corrosion at the neck-stem junction as a cause of metal ion release and pseudotumour formation. J Bone Joint Surg Br 2012;94:895–900. doi:10.1302/0301-620X.94B7.29122.

[24] Goldberg J. The electrochemical and mechanical behavior of passivated and TiN/AlN-coated CoCrMo and Ti6Al4V alloys. Biomaterials 2004;25:851–64. doi:10.1016/S0142-9612(03)00606-9.

[25] Goldberg JR, Gilbert JL. In vitro corrosion testing of modular hip tapers. J Biomed Mater Res B Appl Biomater 2003;64:78–93. doi:10.1002/jbm.b.10526.

[26] Brown SA, Flemming CA, Kawalec JS, Placko HE, Vassaux C, Merritt K, et al. Fretting corrosion accelerates crevice corrosion of modular hip tapers. J Appl Biomater 1995;6:19–26. doi:10.1002/jab.770060104.

[27] Baxmann M, Jauch SY, Schilling C, Blömer W, Grupp TM, Morlock MM. The influence of contact conditions and micromotions on the fretting behavior of modular titanium alloy taper connections. Med Eng Phys 2013;35:676–83. doi:10.1016/j.medengphy.2012.07.013.

[28] Rehmer A, Bishop NE, Morlock MM. Influence of assembly procedure and material combination on the strength of the taper connection at the head-

neck junction of modular hip endoprostheses. Clin Biomech (Bristol, Avon) 2012;27:77–83. doi:10.1016/j.clinbiomech.2011.08.002.

[29] Jennings JM, Dennis DA, Yang CC. Corrosion of the Head-neck Junction After Total Hip Arthroplasty 2016;24:349–56.

[30] Bishop N, Witt F, Pourzal R, Fischer A, Rütschi M, Michel M, et al. Wear patterns of taper connections in retrieved large diameter metal-on-metal bearings. J Orthop Res 2013;31:1116–22. doi:10.1002/jor.22326.

[31] Hothi HS, Panagiotopoulos AC, Whittaker RK, Bills PJ, McMillan R, Skinner JA, et al. Damage Patterns at the Head-Stem Taper Junction Helps Understand the Mechanisms of Material Loss. J Arthroplasty 2016. doi:10.1016/j.arth.2016.06.045.

[32] Jauch SY, Huber G, Sellenschloh K, Haschke H, Baxmann M, Grupp TM, et al. Micromotions at the taper interface between stem and neck adapter of a bimodular hip prosthesis during activities of daily living. J Orthop Res 2013;31:1165–71. doi:10.1002/jor.22354.

[33] Nassif N, Nawabi D, Stoner K, Elpers M, Wright T, Padgett DE. Taper design affects failure of large-head metal-on-metal total hip replacements. Clin Orthop Relat Res 2014;472:564–71. doi:10.1007/s11999-013-3115-3.

[34] Mroczkowski ML, Hertzler JS, Humphrey SM, Johnson T, Blanchard CR. Effect of impact assembly on the fretting corrosion of modular hip tapers. J Orthop Res 2006;24:271–9. doi:10.1002/jor.20048.

[35] Jacobs JJ. Corrosion at the Head-Neck Junction : Why Is This Happening Now ? J Arthroplasty 2016;31:1378–80. doi:10.1016/j.arth.2016.03.029.

[36] Jani S, Sauer W, Mclean T, Lambert R, Kovacs P. Fretting corrosion mechanisms at modular implant interfaces. ASTM Spec Tech Publ 1997;STP 1301:211–25.

[37] Schmidt A, Loch D, Bechtold J, Kyle R. Assessing Morse taper function: the relationship between impaction force, disassembly force, and design variables. ASTM Spec Tech Publ 1997;1301:114–26.

[38] Chana R, Esposito C, Campbell P a, Walter WK, Walter WL. Mixing and matching causing taper wear: corrosion associated with pseudotumour formation. J Bone Joint Surg Br 2012;94:281–6. doi:10.1302/0301-620X.94B2.27247.

[39] Donaldson FE, Coburn JC, Siegel KL. Total hip arthroplasty head-neck contact mechanics: a stochastic investigation of key parameters. J Biomech 2014;47:1634–41. doi:10.1016/j.jbiomech.2014.02.035.

[40] Jauch SY, Huber G, Hoenig E, Baxmann M, Grupp TM, Morlock MM. Influence of material coupling and assembly condition on the magnitude of micromotion at the stem-neck interface of a modular hip endoprosthesis. J Biomech 2011;44:1747–51. doi:10.1016/j.jbiomech.2011.04.007.

[41] Kop A, Keogh C, Swarts E. Proximal component modularity in THA--at what cost? An implant retrieval study. Clin Orthop Relat Res 2012;470:1885–94.

[42] Dunbar M. The proximal modular neck in THA: a bridge too far: affirms. Orthopedics 2010;33:640. doi:10.3928/01477447-20100722-30.

[43] Kop A, Swarts E. Corrosion of a hip stem with a modular neck taper junction: a retrieval study of 16 cases. J Arthroplasty 2009;24:1019–23. doi:10.1016/j.arth.2008.09.009.

[44] Bryant M, Ward M, Farrar R, Freeman R, Brummitt K, Nolan J, et al. Failure analysis of cemented metal-on-metal total hip replacements from a single centre cohort. Wear 2013;301:226–33.
[45] Trentani L, Pelillo F, Pavesi FC, Ceciliani L, Cetta G, Forlino A. Evaluation of the TiMo12Zr6Fe2 alloy for orthopaedic implants : in vitro biocompatibility study by using primary human fibroblasts and osteoblasts 2002;23:2863–9.
[46] Zeng P, Rana A, Thompson R, Rainforth WM. Subsurface characterisation of wear on mechanically polished and electro-polished biomedical grade CoCrMo. Wear 2015;332-333:650–61. doi:10.1016/j.wear.2015.02.007.
[47] Büscher R, Fischer A. The pathways of dynamic recrystallization in all-metal hip joints. Wear 2005;259:887–97. doi:10.1016/j.wear.2005.02.036.
[48] Hurricks P l. The mechanism of Fretting - A review 1970;15:389–409.

LEGENDS

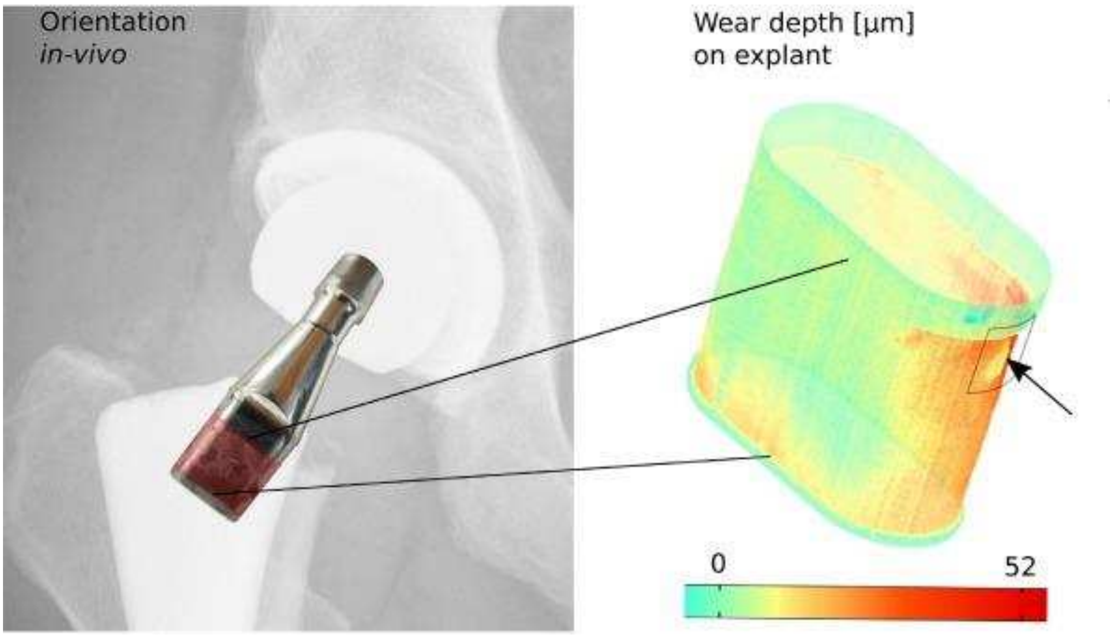

Figure 1: In vivo orientation of wear pattern for a male non-circular neck taper, 26 months in situ. Surface deviations from the estimated pristine geometry are color-coded from green (no deviation) to red (wear). Wear in highly loaded regions exhibited a characteristic pattern, developing around the confined patches at the apex of the conical sections (most prominent medially at the proximal taper end (arrow), but and also diagonally across on the lateral apex).

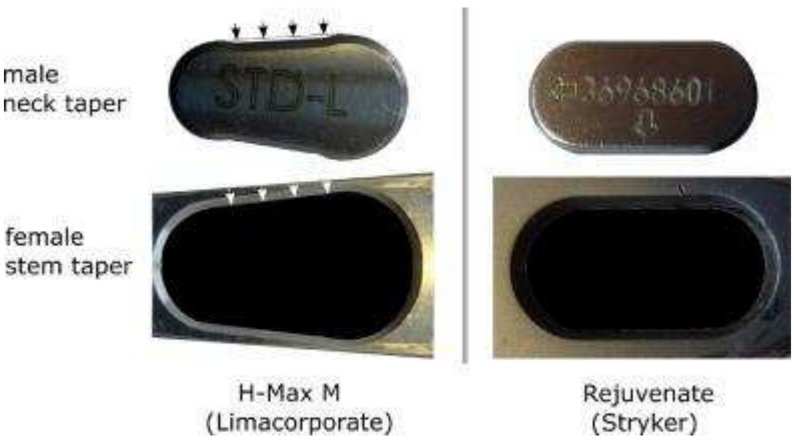

Figure 2: *Top view on two non-circular taper designs with different contact strategies.* ***Left:*** *Undercuts on the flat sides (arrows) macroscopically confines contact regions to conical taper sections (H-Max M, Limacorporate, Villanova di San Daniele (UD), Italy).* ***Right:*** *Specific contact regions cannot be identified on this scale, but will be determined by the taper congruency (Rejuvenate, Stryker Orthopedics, Mahwah, New Jersey).*

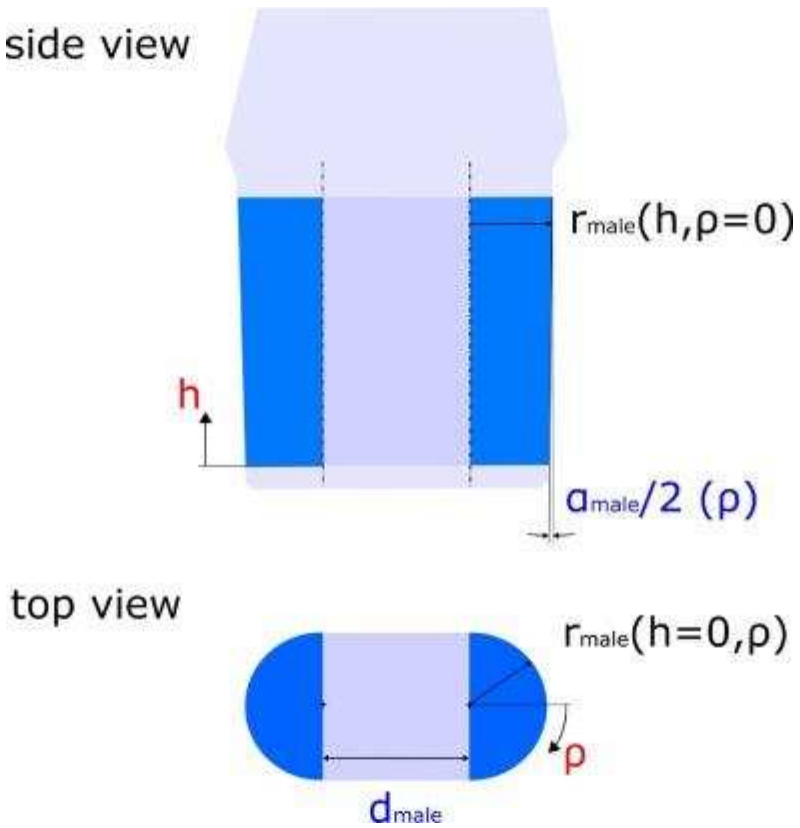

Figure 3: *The parametrization of the bi-modular taper (top: side view; bottom: top view). Two 180° conical sections (height h, radius r, circumferential angle ρ) connected by planes with length d, which corresponds to the distance between the two cone axes. The same parameters are used to describe the male and female tapers. Parameters are computed from averaging*

vertical straightness and horizontal roundness fits on both conical sections (blue; ASTM F3129-16). The connecting planes were not further quantified in geometry.

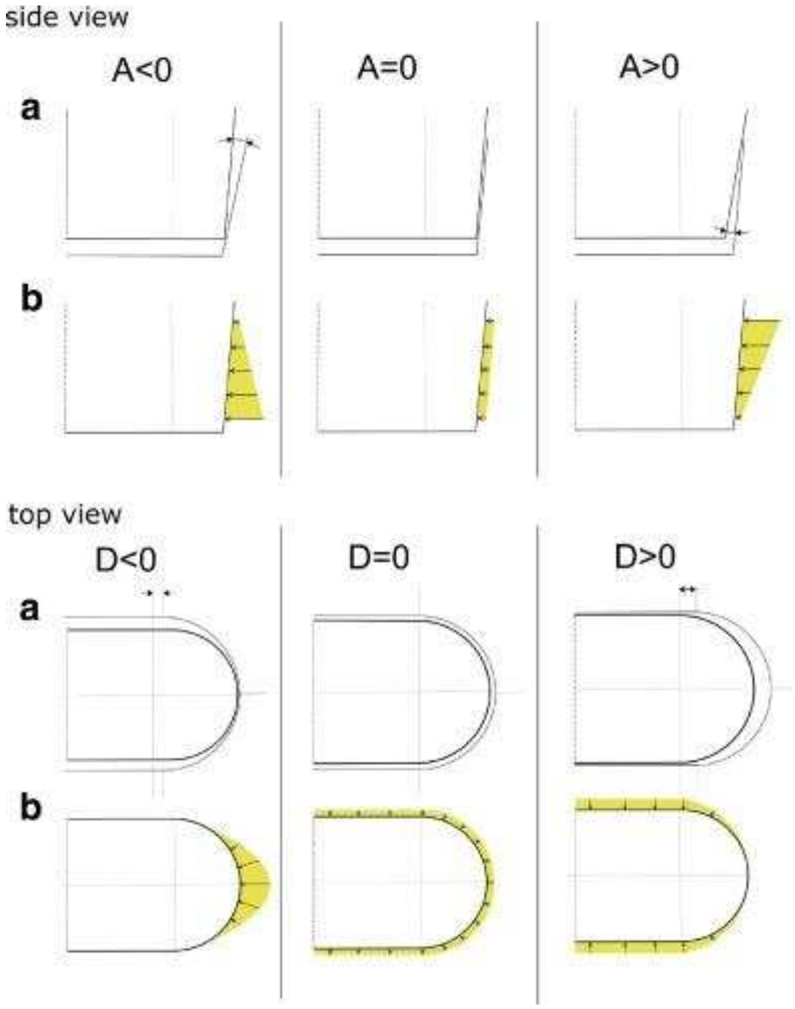

Figure 4: Possible configurations of the engagement and the pre-stress resulting from incongruent non-circular taper geometries. Just one conical apex is shown, since the one on the opposite side behaves similarly. ***Top:*** *The side view reveals the taper angle mismatch A < 0 (throat contact), A = 0 (line contact), and A > 0 (mouth contact).* ***Bottom:*** *The top view reveals the mismatch of conical axes distances D < 0 (apex contact), D = 0 (circumferential contact) and D > 0 (flat contact).* ***a)*** *The engagement of*

the idealized male and female geometry prior to the initial contact ***b)*** *Simplistic estimates for the pre-stress acting on the male taper if pushed into the female taper.*

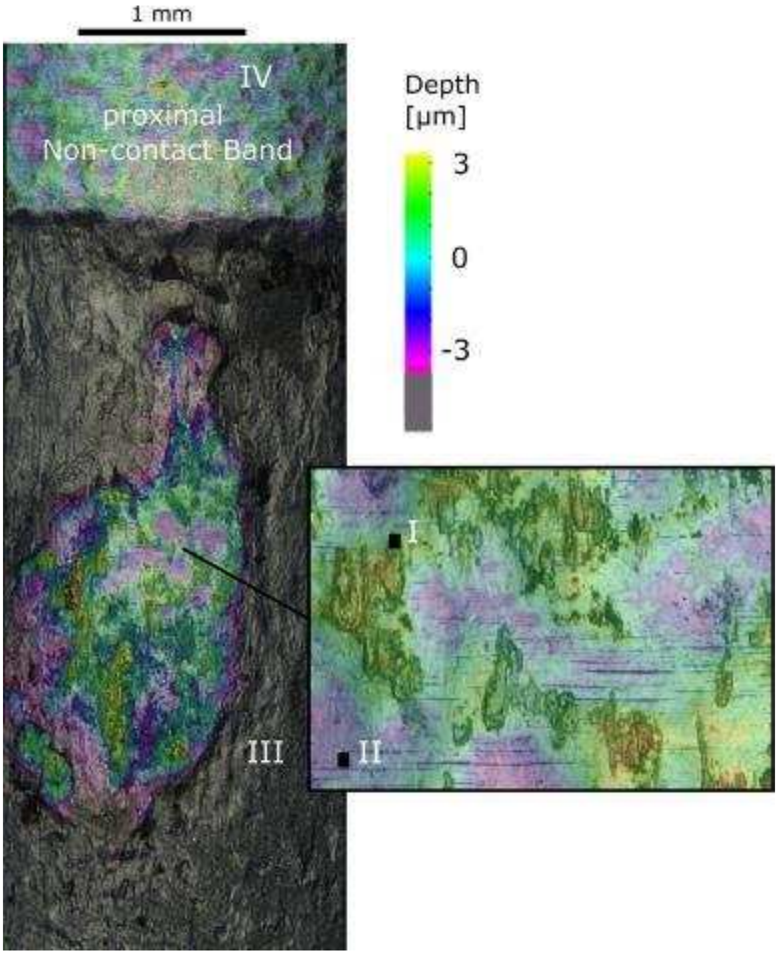

Figure 5: *Material loss around a characteristic patch produced high gradient wear patterns at the proximal tapers' opening. The patches at original surface height were identified at the medial apexes (reference: proximal non-contact band). Distinct locations on one taper were selected, in which site-specific subsurface measurements were performed (sites I & II on the patch, site III at high wear depths, site IV on the non-contact band).*

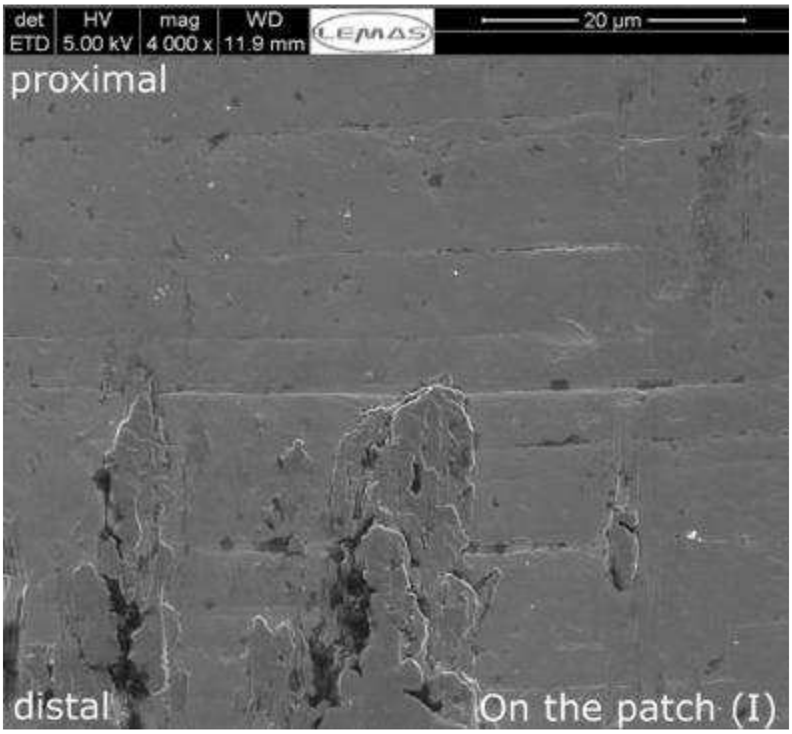

Figure 6: SEM on site I (Figure 5) reveals the original surface texture with intact machining marks and singular deposit.

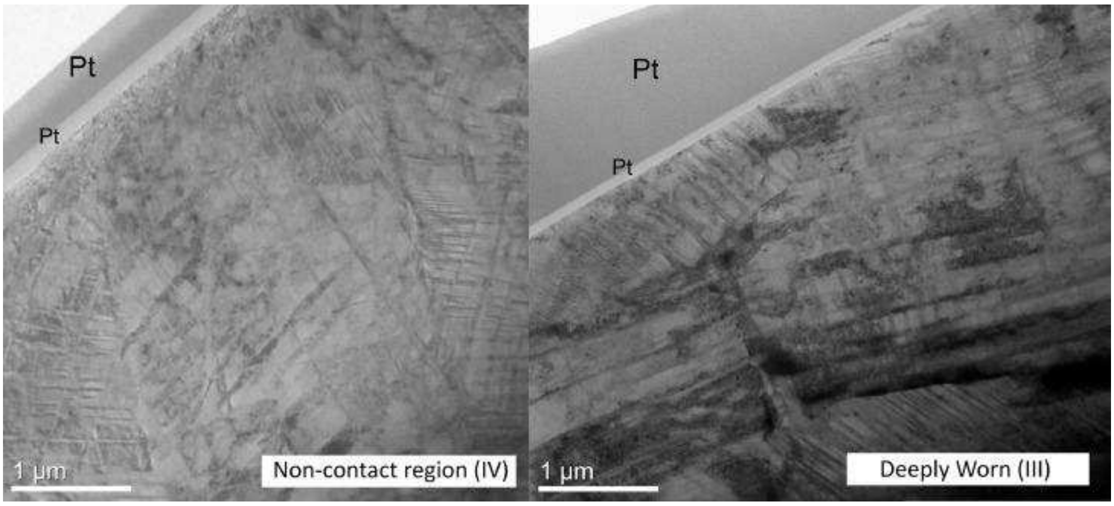

*Figure 7: TEM bright field images showing the microstructure underneath the sputter layer of Platinum (Pt). **Left:** Non-contact site IV. **Right:** Site III of high wear depths in proximity to the medial taper apex. Large grains*

reaching the surface indicate the dominance of corrosive wear in this region.

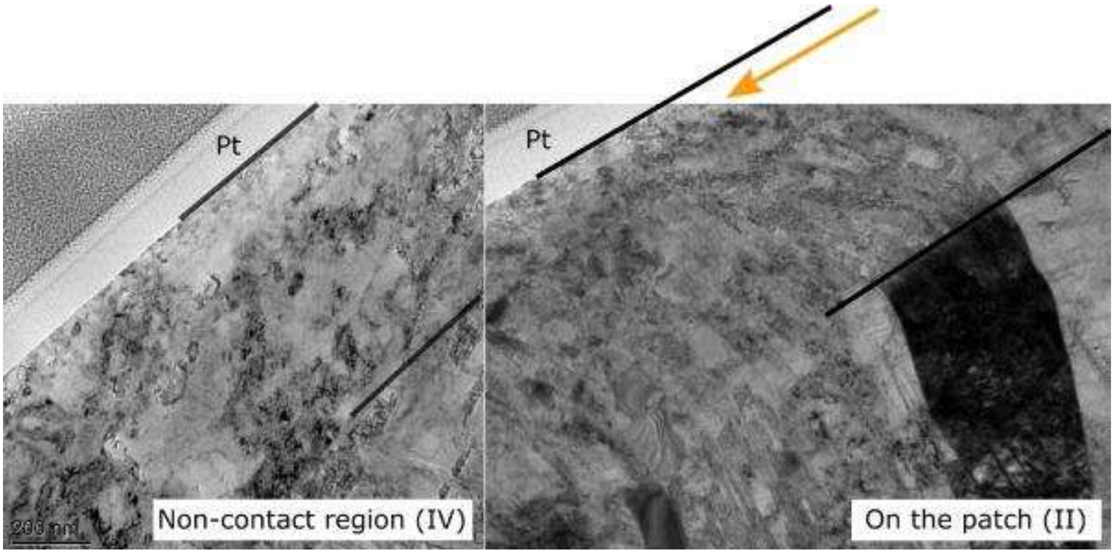

Figure 8: TEM bright field images showing the microstructure underneath the sputter layer of Platinum (Pt). ***Left:*** *Non-contact site IV.* ***Right:*** *Site II on the proximal patch. Black lines were added to indicate the crystalline surface layers. No signs of a corrosive attack to the neck piece material were observed. A collective grain shearing within the uppermost subsurface layers was observed (indicated by an arrow).*

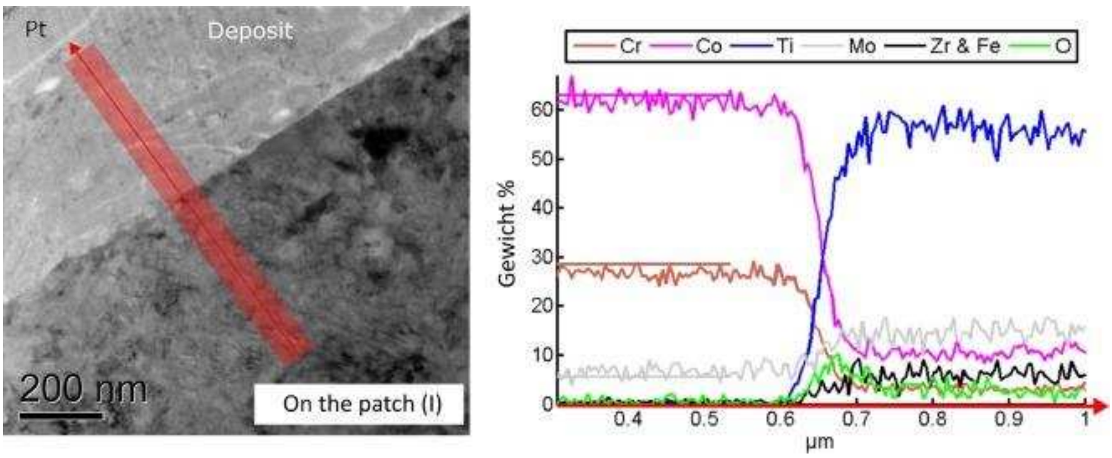

Figure 9: TEM bright field image at site I shows the deposit onto the neck piece material (left), and the element composition scanned across the deposit interface (100 nm wide; right): A transition from CoCr bulk neck alloy (reference lines according to [46]*), separated by an oxygen responsive layer (~100 nm wide) to the deposit containing TMZF bulk alloy elements were recorded. While the Molybdenum content increases to above 10% according to the reported TMZF composition* [45]*, the appearance of Co and Cr content within the deposit remains unclear.*

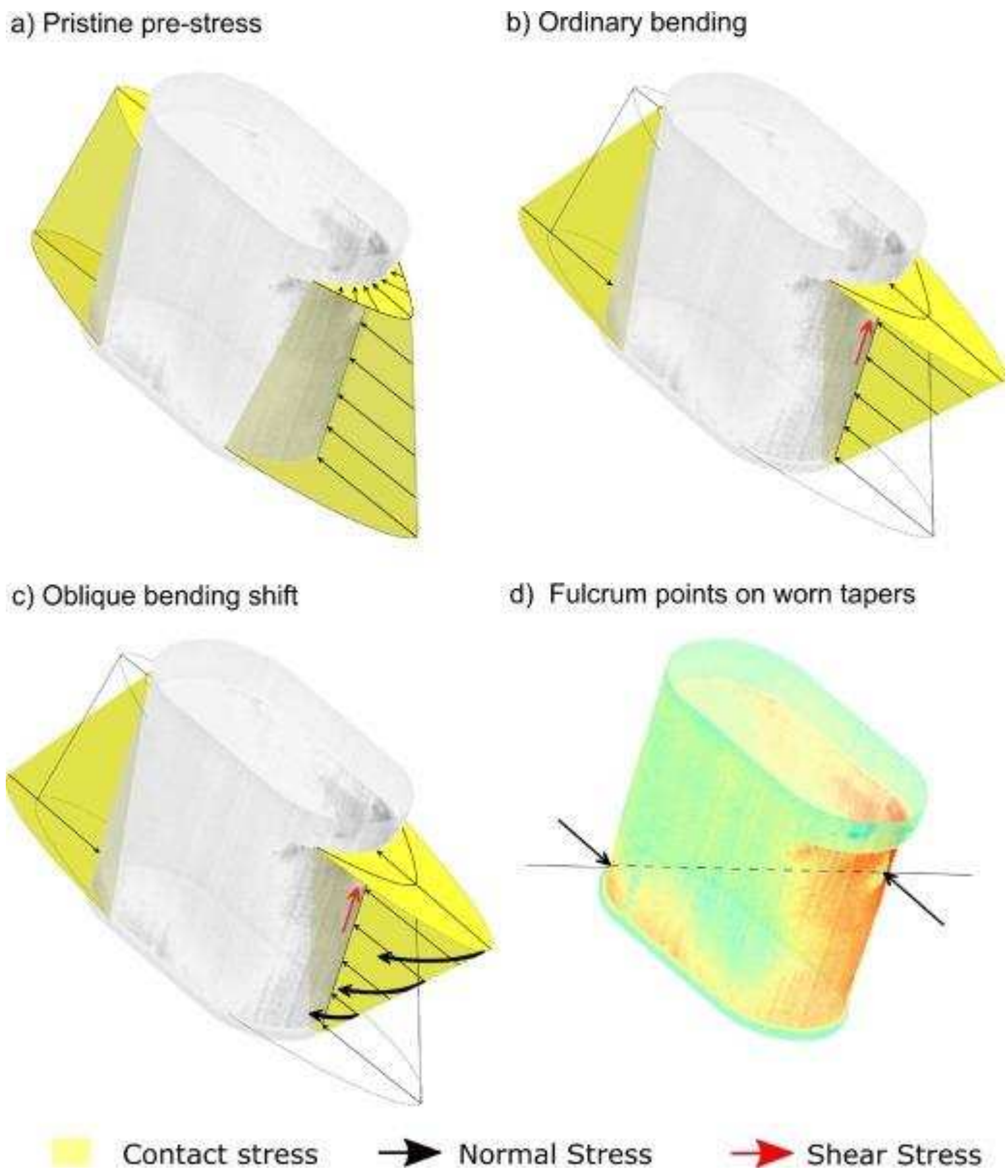

Figure 10: Prediction of the configuration of normal contact stress (yellow) on a male taper of the analyzed design, from pristine to worn. ***a)*** *Initial taper pre-stress in a potential, full apex seating position. Normal stresses (yellow) are expected highest at the apexes, deep inside the taper throat (Figure 3).* ***b)*** *An in vivo load within the longitudinal plane connecting the taper's apexes produces bending in the direction of the taper symmetry plane. In this case, the highest stress will remain at the apexes. The elastic deformation of the components may result in a temporary shift to diagonally distributed contact stresses.* ***c)*** *Loads with an offset to the taper's symmetry plane create an oblique bending. In this case, the highest stress at the taper interface may be tilted from the location of maximal pre-stress available at the apexes. Anterior and posterior flat taper sides may also experience contact loads. At a distance from the apexes, lower pre-stress makes the tapers prone to relative motion.* ***d)*** *Once wear has developed in a diagonal pattern, engaging patches at the conical sections are suspected to act as fulcrum points. Relative motion within the taper is then dominated by a single axis toggling between them.*

Patient	Sex	Implatation side	Age at implantation	Weight	Implant geometry		Time in-situ	Material loss
[#]	M:male F:female	L:left, R:right	[years]	[kg]	Total offset to stem taper [mm]	R: Retroversion A: Anteversion	[months]	[mm^3]
1	F	L	58	74.8	42.6	R	9.1	2.15
2	M	L	44	131.5	44.1	A	36.2	7.57
3	M	R	71	104.3	40.4	A	14.6	0.96
4	M	L	60	78.5	42.6	A	29.3	5.29
5	M	L	61	86.2	42.6	A	10.1	2.13
6	M	R	81	102.1	42.8	A	5.6	3.15
7	M	L	47	117.5	41.3	R	7.2	1.49
8	F	R	65	72.6	45.8	R	7.2	1.67
		L	64	72.6	43.8	R	18.3	2.04
9	M	L	52	90.7	49.7	R	38.1	n.a.*
		R	52	90.7	53.7	R	35.7	2.34
10	M	R	38	86.2	40.1	R	6.2	1.66
11	F	R	66	68.0	42.3	R	18.2	3.58
12	F	L	60	74.8	37.6	A	15.2	4.64
13	F	R	74	99.8	45.1	R	24.0	6.31
14	M	R	65	115.7	45.9	R	32.6	6.64
15	M	R	71	69.9	40.8	R	37.3	n.a.[a]
16	F	L	66	47.2	43.3	A	20.2	0.55
17	F	L	76	61.2	40.6	R	20.3	3.86
	F	R	77	61.2	41.7	R	21.2	4.58
18	M	n.a.	65	86.2	43.5	n.a.	14.2	4.31
		n.a.	65	86.2	41.7	n.a.	14.2	3.02
19	F	L	47	102.1	37.7	R	14.8	2.16
20	F	R	84	45.4	54.1	A	2.9	1.79
21	F	R	75	71.7	42.6	R	21.4	3.09
22	M	L	56	70.3	50.7	R	22.0	4.28
		R	56	70.3	42.8	A	21.5	4.50

a

Excluded from further analyses due to mechanical damage on non-contact reference bands.

Table 1. Patient data and macroscopic implant information of the analyzed cohort. Details on the wear status had been reported elsewhere [18].

Component	Condition	Sample size	Taper angle	Taper axis distance [μm]
Male taper (neck piece)	Retrieved	27	02°58′40″ ± 00′50″	8250 ± 10
	New	4	02°59′00″ ± 00′40″	8251 ± 5
Female taper (stem)	Retrieved	27	03°02′20″ ± 02′20″	8228 ± 10
	New	2	03°01′30″ ± 00′10″	8234 ± 3

Table 2. Global taper angle and taper conical axes distance for cohorts of "new" and "retrieved" tapers (mean and standard deviations).

	Seating depths				
	0 µm	**100 µm**	**200 µm**	**300 µm**	**400 µm**
Proximal gap at the apex of the conical sides	5.2 µm	2.6 µm	0 µm	0 µm	0 µm
Proximal gap at the flat sides	10.2 µm	7.6 µm	4.9 µm	2.4 µm	0 µm

Table 3. Proximal gaps of the unloaded tapers are computed from trigonometrical relations for a mean, idealized taper geometry ($\bar{\alpha}$, d, Table 1). Gap sizes are given for a range of seating depths from first contact (S = 0 µm) to full taper contact (theoretical no gap situation, S = 400 µm).